

Antibacterial Activity and Mechanisms of Magnesium-Doped Baghdadite Bioceramics for Orthopedic Implants

Huu Ngoc Nguyen, Iman Roohani, Andrew Hayles, Zufu Lu, Jitraporn Vongsvivut, Krasimir Vasilev, Vi Khanh Truong,* and Hala Zreiqat*

Baghdadite (BAG, $\text{Ca}_3\text{ZrSi}_2\text{O}_9$), a calcium silicate compound with zirconium incorporation, shows significant potential in medical implants. However, its susceptibility to infections poses a considerable challenge. To tackle this problem, doping biocompatible magnesium (Mg) into BAG to create Mg-BAG enhances antibacterial activity and prevents infection in orthopedic implants. Mg-BAG demonstrates effectiveness against Gram-positive *Staphylococcus aureus* and Gram-negative *Pseudomonas aeruginosa*. This study finds that the antibacterial activity of Mg-BAG is multifaceted including causing the generation of reactive oxygen species (ROS) within cells and disrupting membrane potential, resulting in leakage of intracellular contents. The synchrotron macro attenuated total reflectance Fourier-transform infrared microspectroscopy shows the impact of Mg-BAG on bacteria, resulting in modifications to biomolecules such as lipids, protein structures, and the stability of nucleic acids. The combined effect of Mg ions (Mg^{2+}) and intracellular ROS formation contributes to the disruption of biomolecules and bacterial cell death. Mg-BAG is a promising next-generation bioceramic offering innovative nonantibiotic solutions for preventing infection.

(scaffolds) is the risk of microbial infection, contributing to implant failure. Bacterial colonization on implant surfaces often undermines their functionality. Infection rates are reported to be between 2% and 5% in the case of orthopedic implants,^[1] increasing to a concerning 30% in the case of open fractures.^[1,2] Implant-associated infections (IAIs) are commonly linked to *Pseudomonas aeruginosa* (*P. aeruginosa*) and *Staphylococcus aureus* (*S. aureus*) and pose a challenge to the success of orthopedic implants.^[3] After revision surgery, there is a recurrence rate of around 33% for infections resulting in an increase in treatment cost from \$17 000 to \$150 000 per patient.^[4] Unfortunately, diagnosing an implant infection poses a challenge for success due to the difficulty in eliminating bacteria. Addressing infections with antibiotics proves to be problematic given the concerning rise of antibiotic-resistant organisms.


Traditional approaches such as replacing devices and administering antibiotics for periods unintentionally worsen the growing issue of resistance (AMR).^[5] The World Health Organization predicts that by 2050, AMR could lead to 10 million deaths annually, surpassing the current cancer mortality rate and potentially costing the global economy \$100 trillion if preventive

1. Introduction

Various synthetic materials (e.g., scaffolds) have been created to address the drawbacks of autografts and allografts. However, a significant obstacle hindering the success of these implants

H. N. Nguyen, I. Roohani, Z. Lu, H. Zreiqat
Tissue Engineering and Biomaterials Research Unit
School of Biomedical Engineering
The University of Sydney
Camperdown, NSW 2006, Australia
E-mail: hala.zreiqat@sydney.edu.au

I. Roohani
School of Biomedical Engineering
Faculty of Engineering and Information Technology
University of Technology Sydney
Sydney, NSW 2007, Australia

 The ORCID identification number(s) for the author(s) of this article can be found under <https://doi.org/10.1002/anbr.202400119>.

© 2024 The Author(s). Advanced NanoBiomed Research published by Wiley-VCH GmbH. This is an open access article under the terms of the Creative Commons Attribution License, which permits use, distribution and reproduction in any medium, provided the original work is properly cited.

DOI: 10.1002/anbr.202400119

A. Hayles, K. Vasilev, V. K. Truong
Biomedical Nanoengineering Laboratory, College of Medicine and Public Health
Flinders University
Bedford Park, SA 5042, Australia
E-mail: vikhanh.truong@flinders.edu.au

J. Vongsvivut
Infrared Microspectroscopy Beamline
ANSTO Australian Synchrotron
Clayton, VIC 3168, Australia

V. K. Truong
Healthcare Engineering Innovation Group (HEIG)
Department of Biomedical Engineering and Biotechnology, College of Medicine and Health Sciences
Khalifa University of Science and Technology
Abu Dhabi, UAE

measures are not implemented.^[6] Thus, there is an urgent need to develop and design next-generation antimicrobial synthetic bioceramics for effective prevention and minimizing the risk of IAIs.

The increasing interest in baghdadite (BAG, $\text{Ca}_3\text{ZrSi}_2\text{O}_9$) as a synthetic bone substitute can be attributed to its properties, such as bioactivity, biodegradability, and ability to support the healing of large bone defects.^[7] However its effectiveness in preventing bacterial growth is limited. Current strategies involve the use of transition-metal ions such as copper (Cu^{2+}), zinc (Zn^{2+}), and silver (Ag^+), which show varying degrees of success, against bacteria.^[8] Some studies developed on creating Ag^+ and Cu^{2+} coatings for implants to inhibit bacterial growth disrupt bacterial cell membranes, interfere with essential cellular processes, and prevent biofilm formation.^[9] However, the use of Ag^+ and Cu^{2+} is limited by concerns about their toxicity^[10] and the potential for the development of antibiotic resistance.^[11]

Previous research has reported that incorporating magnesium (Mg) into BAG can improve its mechanical strength and biological properties, benefiting bone tissue engineering.^[12] Additionally, magnesium ions play a role in biological processes such as promoting bone formation (osteogenesis) and the development of blood vessels (angiogenesis), both vital for effective bone healing. By incorporating magnesium into BAG (Mg-BAG), the ability of the material to support in vitro and in vivo bone repair is significantly enhanced by promoting cell adhesion and growth and stimulating the mineralization of the matrix for better integration with natural bone tissue.^[7e,12,13] Furthermore, Mg^{2+} has reported bactericidal and bacteriostatic potential.^[14] Magnesium ions work by disrupting membranes and interfering with their functions making them effective against bacteria. In addition, they offer cost-effective antibacterial properties and biocompatibility.^[14a–e] This study investigates the effectiveness of Mg-BAG in preventing infections.

The surface topography of biomaterials is recognized to influence bone integration and the adhesion of bacteria^[3a,15] while implant surface microroughness has been shown to promote bone cell proliferation and osteogenic differentiation,^[16,17] it can also increase the risk of infections.^[18] In contrast, nano-roughness topographies may have the ability to eliminate microbes by disrupting their cell walls.^[19] However, the relationship between surface roughness and cellular adhesion remains a topic of debate with studies showing varying results.

This study aims to investigate the antimicrobial properties of Mg-BAG against commonly orthopedic implant-related pathogens *P. aeruginosa* and *S. aureus*. We further explored the antimicrobial effect in response to the nano- and micro-scale surface topographies of Mg-BAG and the multifaceted antibacterial mechanisms involved in this response, including alterations to biomolecules, the generation of intracellular reactive oxygen species (ROS), and membrane depolarization, ultimately leading to disrupting bacterial membrane integrity.

2. Results and Discussion

2.1. Fabrication and Characterization of Magnesium-Doped Baghdadite

We synthesized bioceramic BAG discs with the dimensions of 14 mm diameter and $\times 2$ mm height using a solid-state synthesis

method, Mg is a dopant, as described in **Figure 1** and Figure S1, Supporting Information.^[12,13] The approach enables precise control over the doping of Mg into BAG via substituting Zr^{2+} or Ca^{2+} with divalent Mg^{2+} . The successful doping of Mg into BAG was demonstrated through spectroscopic techniques including energy-dispersive X-ray spectroscopy (EDS), X-ray photoelectron spectroscopy (XPS), and X-ray diffraction (XRD) analysis shown in **Figure 2A–C**. Elemental mapping of the Mg-BAG surface discovered a distribution of Ca, Zr, Si, O, and Mg. The uniform distribution of these elements across Mg-BAG surfaces, confirmed through EDS analysis, provides evidence of the successful synthesis process that is achieved via homogenous doping of Mg throughout the surfaces. Additionally, detecting the Mg 1s peak in Mg-BAG indicates the successful integration of Mg, confirming the effective synthesis of the Mg-BAG.

The microscale and submicroscale topographies of the implant surface play a role in the initial bacterial attachment and the biofilm formation.^[20] In this study, the sample surfaces were polished to a smooth finish. We used 3D profilometry to assess the surface texture of hydroxyapatite (HAp), BAG, and Mg-BAG, as illustrated in Figure 2D and detailed in Table S1, Supporting Information. The unpolished surfaces referred to as “rough,” for HAp BAG and Mg-BAG, showed areas at a scale with average roughness (R_a) values of 1.264 ± 0.051 , 1.932 ± 0.268 , and $1.640 \pm 0.180 \mu\text{m}$, respectively. On the other hand, the polished surface known as “smooth” had features at a scale with significantly lower R_a values of $0.115 \pm 0.002 \mu\text{m}$ for HAp, $0.347 \pm 0.017 \mu\text{m}$ for BAG, and $0.223 \pm 0.010 \mu\text{m}$ for Mg-BAG.

2.2. Assessing the Antibacterial Activity of Mg Incorporation and Surface Topography Optimization for Improved Antibacterial Activity

We evaluated the antibacterial performance of HAp, BAG, and Mg-BAG, specifically targeting their impact on Gram-negative *P. aeruginosa* and Gram-positive *S. aureus*. These two pathogens are strongly associated with IAIs.^[3] The BacLight Live/Dead fluorescent dye assay was used to evaluate the viability of cells based on the integrity of their membranes on surfaces.^[21] Our results indicated that BAG displayed activity leading to roughly 12% of cells being dead while HAp showed no bactericidal effect against *P. aeruginosa* or *S. aureus* (**Figure 3**). In contrast, after a three-hour incubation, both Mg-BAG showed a notable increase in dead cells compared to BAG and HAp, with $\approx 75\%$ of the population being affected for both bacterial strains ($p < 0.001$). Extending the incubation time to six hours did not increase the percentage of cells indicating that Mg-BAG can effectively inhibit most bacteria within the first three hours of exposure. Additionally, the roughness of the surface did not significantly impact the bactericidal properties of Mg-BAG.

In order to investigate if the antibacterial effects we observed were dependent on contact we conducted the disk diffusion assay (Figure 3C).^[22] The BAG bioceramic, regardless of being smooth or rough, showed minimal inhibition zones ($\approx 0.7 \pm 0.55$ mm) against *P. aeruginosa* and exhibited no inhibition zone against *S. aureus*. On the other hand, our engineered Mg-BAG demonstrated significant inhibition zones ranging from 3.33 ± 1.52 to 4.00 ± 1.00 mm against both *P. aeruginosa* and *S. aureus* as

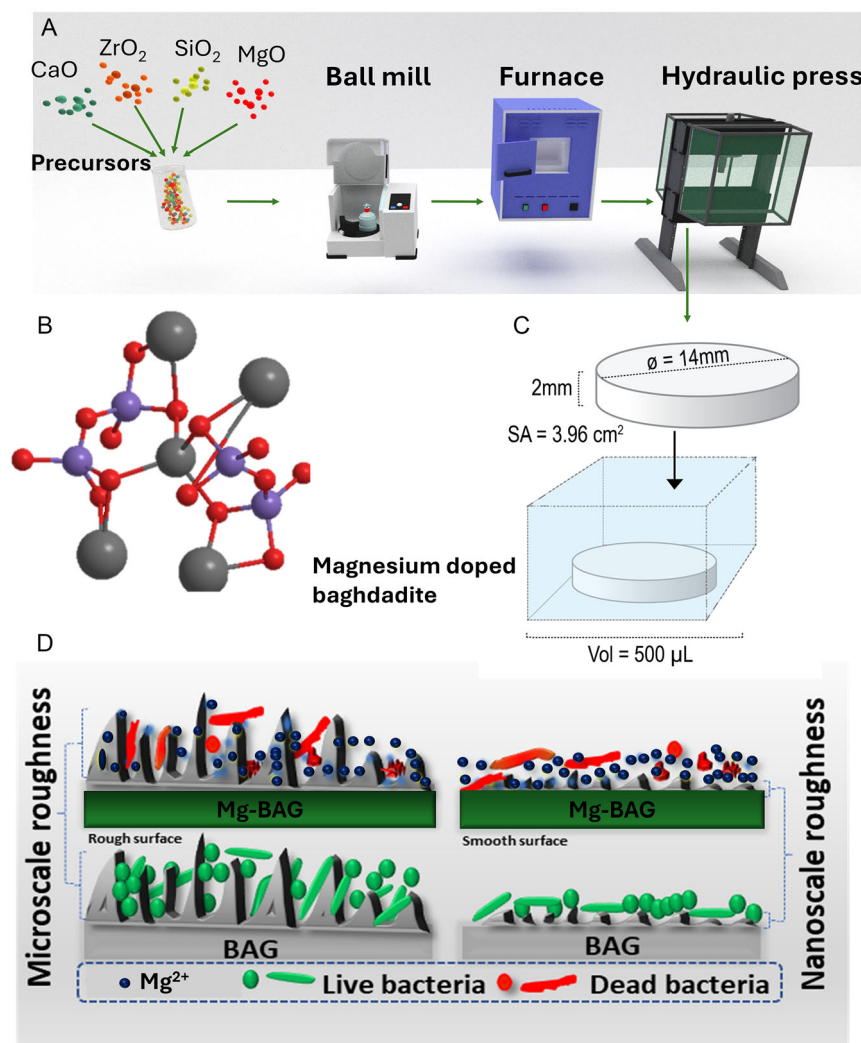


Figure 1. Schematic of magnesium-doped baghdadite (Mg-BAG) fabrication. A) The synthesis process of Mg-BAG starts from mixing precursors in a ball mill, then sintering in a furnace, and forming into discs using a hydraulic press. B) Molecular structure of Mg-BAG with the arrangement of Ca, Zr, Si, Mg, and O atoms. C) Representation of a disc-shaped magnesium-doped baghdadite sample, detailing dimensions (diameter = 14 mm, thickness = 2 mm) and surface area ($SA = 3.96 \text{ cm}^2$). D) Comparison of microscale and nanoscale surface roughness on Mg-BAG and BAG, demonstrating the interaction with live and dead bacteria.

detailed in Figure S3 and Table S2, Supporting information. These findings align with our previous observation that the antibacterial effectiveness of Mg-BAG is not influenced by surface roughness.

Although bacterial resistance to heavy metals such as Cd,^[23] Zn,^[24] Ag,^[25] and Cu^[26] through efflux systems has been well-documented, no resistance specifically to Mg has been reported. This investigation revealed that the antibacterial activity of Mg-BAG could effectively kill both *S. aureus* and *P. aeruginosa*. Importantly, this effect was observed regardless of the surface roughness of the doped BAG samples. This outcome is promising because surface roughness is a property that facilitates bone integration,^[27] but also promotes bacterial attachment.^[28]

The period right after bacteria attach is crucial, in determining if an infection will occur.^[29] This early-stage action is critical in clinical scenarios where rapid infection prevention is required

for successful implant integration.^[30] The ions released from Mg-BAG interact with and disrupt processes within bacteria leading to damage and ultimately bacterial death. Gram-negative and Gram-positive bacteria have cell surfaces that are negatively charged due to components like the peptidoglycan layer, lipopolysaccharides, and phosphate groups in the cell envelope. This charge facilitates the binding of metal ions.^[31] Research on how ions are released from Mg-BAG samples shows that magnesium ions are released from the surfaces of the doped glass, contributing to their combined antibacterial effect.

Our previous research has shown that Mg-BAG is highly biocompatible and bioactive.^[12] This combination of properties, along with antibacterial effectiveness, makes Mg-BAG bioceramics promising for use in applications. Additionally, their antibacterial properties could be especially beneficial for patients or in situations where there is a risk of infection.

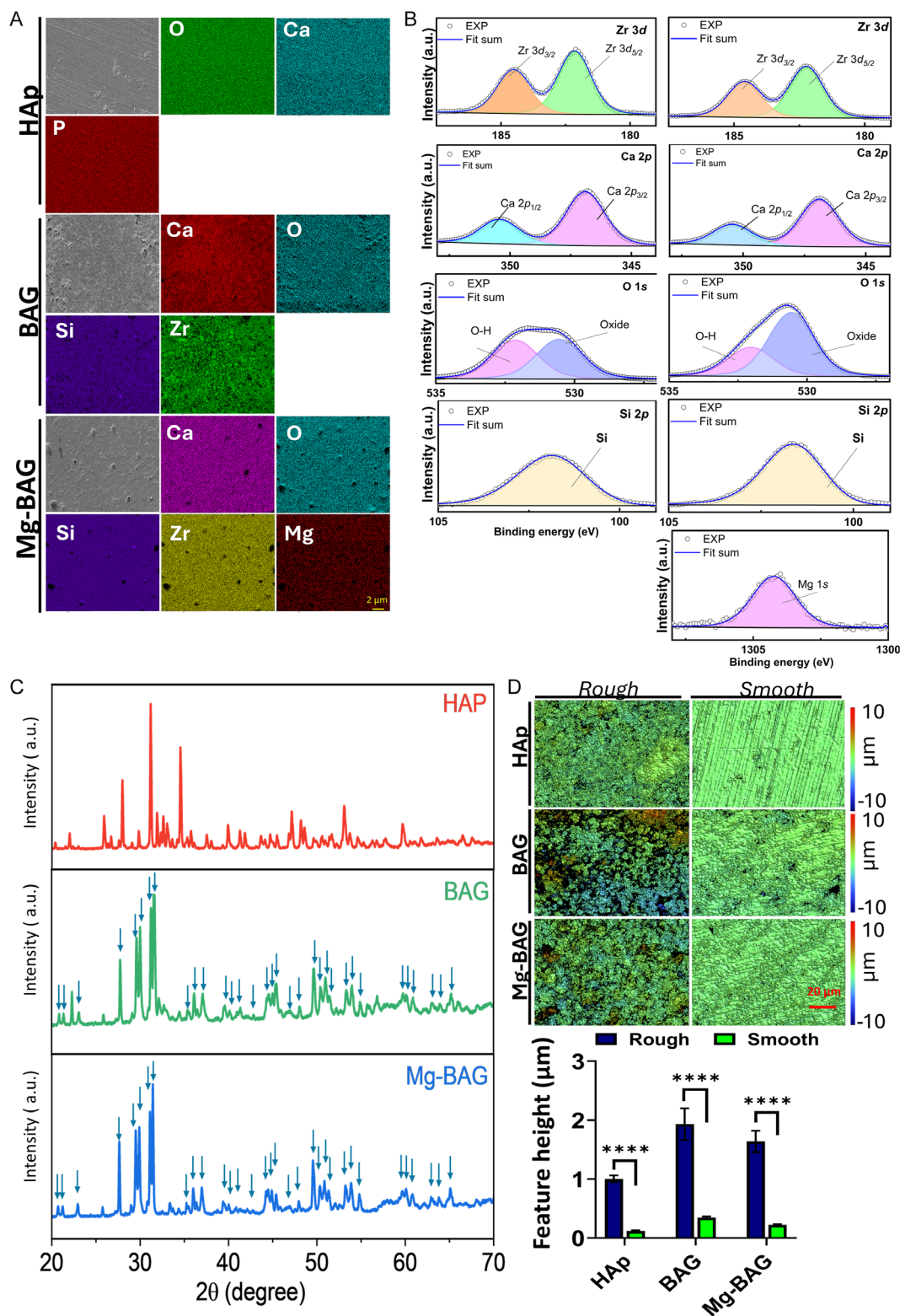


Figure 2. Compositional and surface roughness analysis of HAp, BAG, and Mg-BAG. A) EDS mapping reveals the distribution of elements on the sample surfaces. B) XPS spectra provide insights into the elemental makeup and chemical states of Zr, Ca, Si, and Mg. C) XRD patterns illustrate the diffraction angles and intensities associated with the crystalline phases, found in the samples. D) Detailed surface topography analysis conducted using 3D profilometry. $n = 3 \pm$ standard deviation (SD), **** $p < 0.0001$.

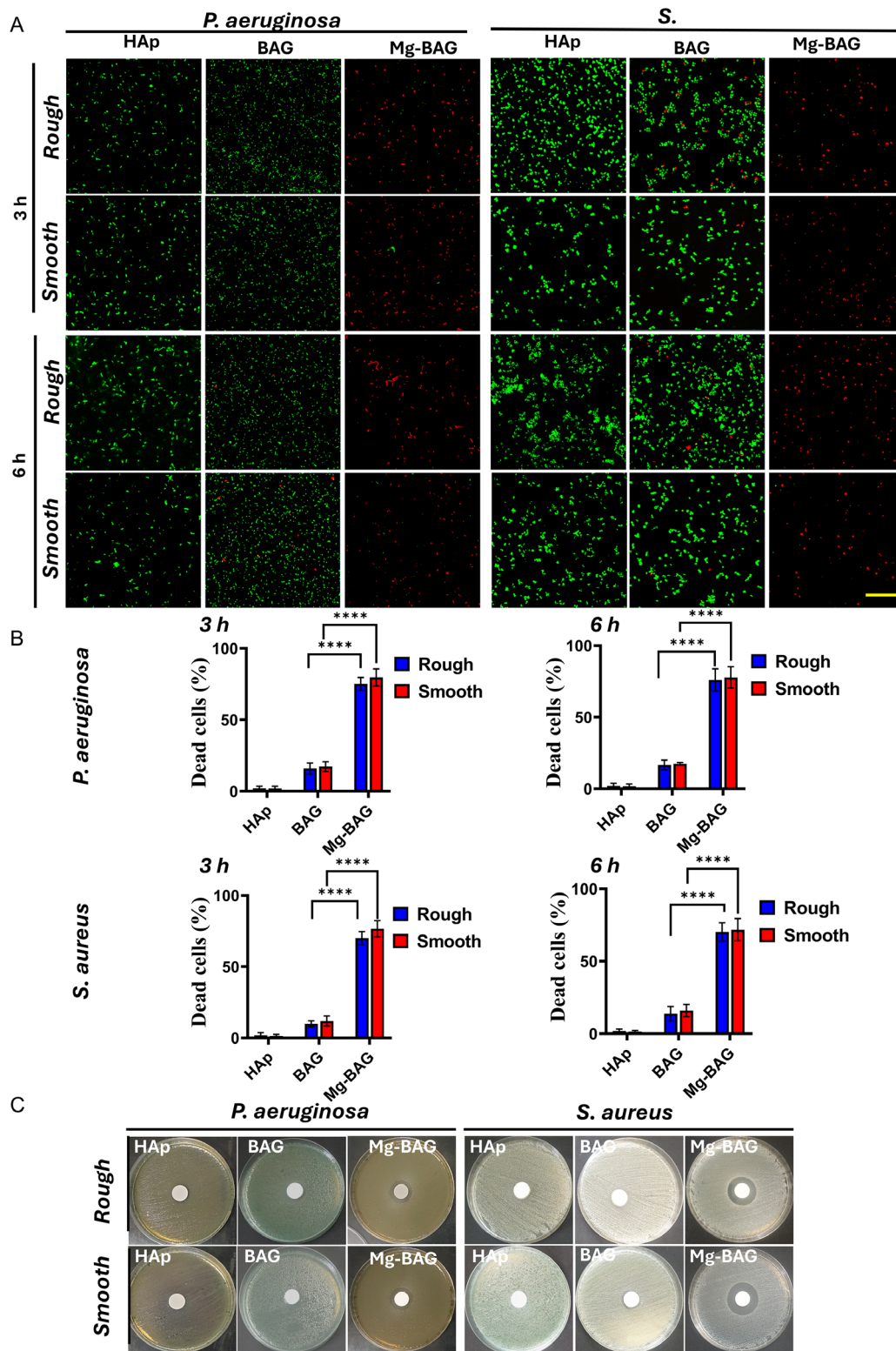


Figure 3. Evaluating the antibacterial efficacy of HAp, BAG, and Mg-BAG, against *P. aeruginosa* and *S. aureus*. A) Live/dead fluorescence micrographs depicting *P. aeruginosa* and *S. aureus* incubated on HAp, BAG, and Mg-BAG surfaces for 3 or 6 h, providing visual evidence of antibacterial activity. Green and red fluorescent spots represent live and dead bacteria, respectively. The scale bar represents 20 μm . B) Quantitative analysis of bacterial cell viability derived from the fluorescence micrographs, illustrating the comparative effectiveness of the samples. C) Zone of inhibition assay underscoring the antibacterial properties of Mg-BAG. $n = 3 \pm \text{SD}$, **** $p < 0.0001$.

2.3. Study Antibacterial Mechanisms of Mg-BAG

Previous studies have demonstrated that Mg^{2+} can be used for antibacterial properties because it enhances the production of ROS, disrupts bacterial metabolic processes by interacting with the negatively charged bacterial cell wall and membrane components, and creates an alkaline environment that hinders bacterial growth.¹⁴ To investigate the ion release rate from Mg-BAG, we employed inductively coupled plasma mass spectrometry (ICP-MS) to quantify the ion concentrations for 3, 6, and 24 h, as shown in Figure 4B. Interestingly, no significant differences were observed in ion release rate across surfaces. We observed

Mg^{2+} concentration of 7.8 ppb mm^{-3} after 3 h, increasing to 10 ppb mm^{-3} at 6 h and then 11 ppb mm^{-3} at 24 h for Mg-BAG samples.

The study of the morphologies of *S. aureus* and *P. aeruginosa* on modified bioceramics was conducted using microscopy scanning electron microscopic (SEM) as shown in Figure 4C. Both bacterial strains showed changes in appearance on the smooth and rough surfaces of Mg-BAG. Specifically, the bacteria exhibited wrinkled, uneven, and irregular shapes when interacting with Mg-BAG. These alterations seemed to result in Mg^{2+} ions interacting with the negatively charged bacterial cell wall and membrane components, compromising their integrity and

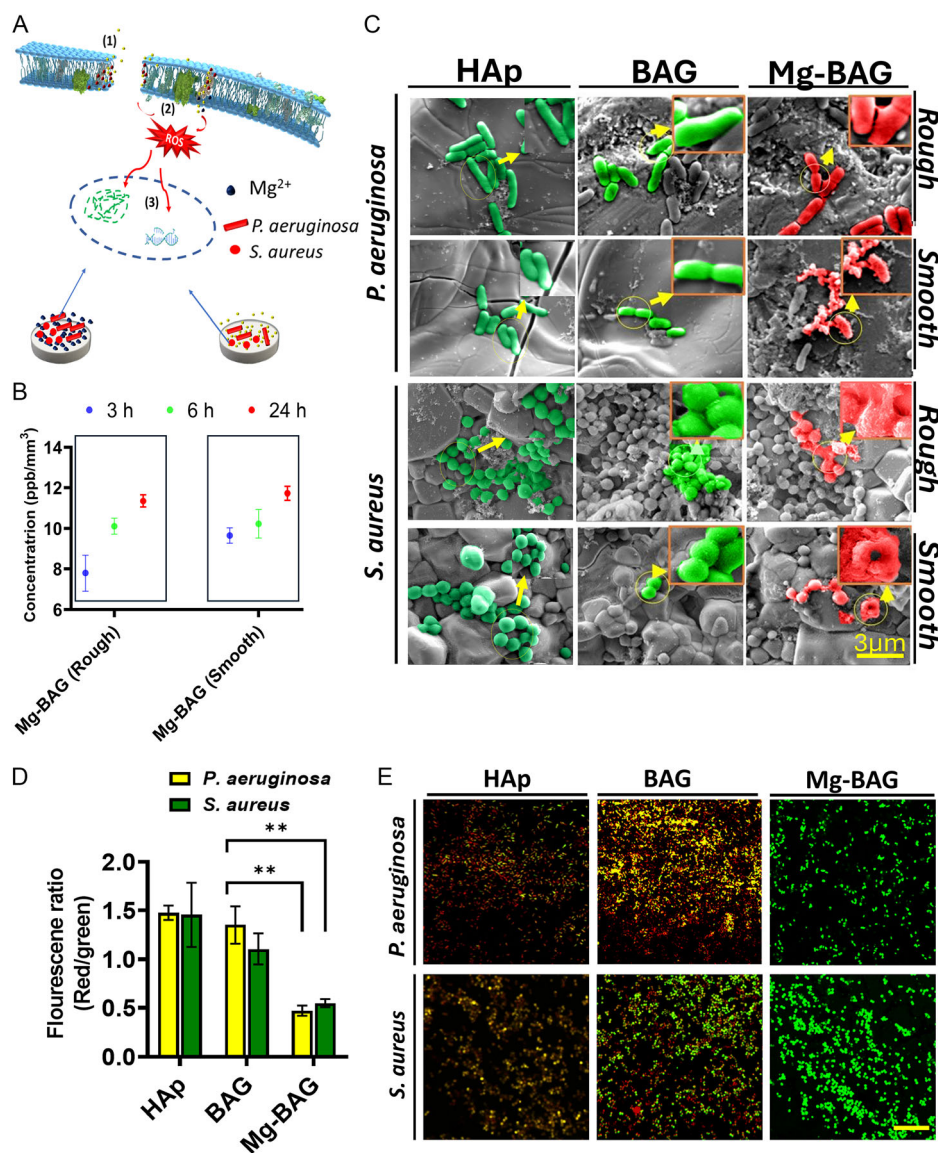


Figure 4. The multifaceted antibacterial mechanisms of Mg-BAG bioceramics. A) Schematic representation of multitarget mechanisms of antibacterial action of Mg-BAG. B) Quantification of Mg^{2+} -ion release from rough and smooth surfaces of Mg-BAG over time. C) SEM images illustrate these altered morphologies of bacteria exposed to Mg-BAG, including wrinkled, uneven, and irregular shapes and swollen cells exhibiting signs of damage. D) Membrane potential of *P. aeruginosa* and *S. aureus*. E) CLSM micrographs of *P. aeruginosa* and *S. aureus* on doped bioceramics. Green fluorescence indicates a high degree of membrane polarization. The scale bar represents $20 \mu\text{m}$. $n = 3 \pm \text{SD}$, $**p < 0.01$.

function. In contrast, bacteria exposed to HAp and BAG retained their original morphologies, maintained their shape, and preserved their membrane structure.

To assess the mechanism behind the antibacterial effectiveness of Mg-BAG, we examined the membrane potential of both bacteria after exposure to HAp, BAG, and Mg-BAG surfaces. This was done using the BacLight bacterial membrane potential kit. Ion pumps like the Na/K ATPase pump and the proton pumps (H^+ -ATPase) in bacteria are essential for maintaining the gradient across the cell membrane.^[32] This gradient is crucial for functions such as ATP production and nutrient absorption and contributes to a high membrane potential. Magnesium ions (Mg^{2+}) can interfere with the function of ion pumps by disrupting their normal operation. Mg^{2+} competes with ions like calcium (Ca^{2+}) and potassium (K^+) at binding sites in ATP-dependent pumps such as Na^+/K^+ ATPase. When Mg^{2+} binds to channels or pumps, it can change the shapes of these transport proteins reducing their effectiveness in maintaining ion gradients. Specifically, Mg^{2+} inhibits pumps that create proton gradients necessary for ATP production and energy generation.

Bacterial cells with functioning ion pumps preserve a membrane potential, indicated by a red fluorescence signal from the accumulation of the DiOC₂(3) dye in polarized cells. Conversely, when ion pumps are compromised by Mg^{2+} there is a depolarization of the membrane, leading to a shift toward green fluorescence observed in cells exposed to Mg-BAG surfaces (Figure 4D,E). This shift signifies disrupted ion homeostasis further illustrating how Mg^{2+} impairs the integrity and function of bacterial membranes.^[33] Thus, green fluorescence signifies bacteria with membranes, while red fluorescence indicates a membrane potential commonly observed in healthy, energized cells. Our results demonstrate depolarization in bacteria exposed to Mg-BAG bioceramic, suggesting a disruption in membrane integrity. An analysis of bacterial samples adhering to BAG showed a red-to-green fluorescence ratio of ≈ 1.4 . In contrast, on the Mg-BAG, the ratio decreased to around 0.5, indicating a compromised membrane potential due to disrupted ion pumps.

In the presence of ROS, the compound 2',7'-dichlorodihydrofluorescein diacetate undergoes oxidation into a highly fluorescent form known as ',7'-dichlorofluorescein. This transformation enables the measurement of levels of ROS as illustrated in Figure 5A. ROS are normally generated when metal ions (Mg^{2+}) interact with cellular components to initiate redox reactions, leading to the formation of ROS like superoxide anions (O_2^-), hydroxyl radicals ($OH\cdot$), and hydrogen peroxide (H_2O_2).^[34] Our research findings indicated no ROS detected within *P. aeruginosa* and *S. aureus* cells growing on BAG surfaces (see Figure 5B,C). Remarkably, exposure to Mg-BAG surfaces resulted in a marked 3–4-fold elevation of ROS production in both bacterial species, regardless of the roughness of the surface. This indicates that releasing Mg^{2+} ions from Mg-BAG surfaces induces ROS generation resulting in their damage due to oxidative stress.

Mg^{2+} can indirectly bring up ROS generation through a redox reaction.^[35] In the context of Mg^{2+} , cellular enzymes, including NADPH oxidase, are activated and capable of accepting electrons to molecular oxygen (O_2), leading to superoxide anion (O_2^-) generation. The Fenton reaction can also occur with the involvement

of Mg^{2+} , in which hydrogen peroxide converts into highly reactive hydroxyl radicals.^[36] These ROS can deliver oxidative stress to the bacterial cell, damaging lipids, proteins, and DNA, causing homeostasis dysregulation. It may cause leakage of cellular content as well as a disequilibrium on ion gradients inducing cell death. Therefore, the interaction between Mg^{2+} release, membrane disruption and ROS generation remarkably increases the antibacterial activity of these Mg BAG surfaces, which strongly supports their applications as potent infective bacteria-controlling biomaterials.

The localized alteration in pH occurs due to the release of Mg^{2+} ions from the material. When magnesium interacts with the environment, magnesium hydroxide is produced ($Mg(OH)_2$).^[37] This process enhances the levels of alkalinity, leading to antibacterial properties.^[38] Our research into properties uncovered a notable increase in pH levels in a solution containing Mg-BAG as shown in Figure S4, Supporting Information. This alkaline environment, created by releasing ions during the degradation of Mg-BAG, boosts the activity by disrupting their cellular functions that thrive in acidic conditions. The combined impact of the pH, Mg^{2+} release, and ROS formation significantly improves the antibacterial potency of Mg-BAG.

As membrane depolarization can lead to loss of cell contents, we investigated the leakage of nucleic acids and proteins into the supernatant following incubation on Mg-BAG (Figure 6). The results show a significant increase in nucleic acids and proteins in the culture medium from bacteria exposed to Mg-BAG, compared to those on HAp and BAG. These findings highlight the significant impact of Mg-BAG surfaces on releasing nucleic acids and proteins from bacterial cells, indicating a disruption of cell envelope integrity. Interestingly, the actions of Mg-BAG are very similar to those of quaternary ammonium compounds, which are also cationic compounds that kill bacteria by interfering with the cell envelope and causing leakage of cell contents.^[39]

2.4. Variation in Lipids, Proteins, and Nucleic Acids Profiles Observed Using Synchrotron ATR-FTIR Microspectroscopy

The potential enhancement of antibacterial activity by Mg-BAG may be due to a cooperative or synergistic effect arising from releasing metal ions during their contact with the microorganisms. Previous studies show that metal ions play a crucial role in the creation and breakdown of key macromolecules, including carbohydrates, lipids, proteins, and nucleic acids.^[40] Herein, we use synchrotron-sourced macro attenuated total reflectance Fourier-transform infrared (ATR-FTIR) microspectroscopy to elucidate the mechanisms behind the biomolecule changes induced by our Mg-BAG within bacterial cells (Figure 7A and 8A).^[41] By analyzing three spectral regions containing crucial biomolecular information, including the $\nu(C-H)$ stretching modes representing lipid composition ($3000-2850\text{ cm}^{-1}$), the amide I and II bands representing proteins ($1700-1450\text{ cm}^{-1}$), and the vibrational modes related to nucleic acids and polysaccharides ($1150-1000\text{ cm}^{-1}$), this approach provided valuable insights into the structural modifications induced by the Mg-BAG on bacterial cells.

The resulting heat maps displayed variations in intensity within these spectral regions (Figure 7B and 8B). Despite the

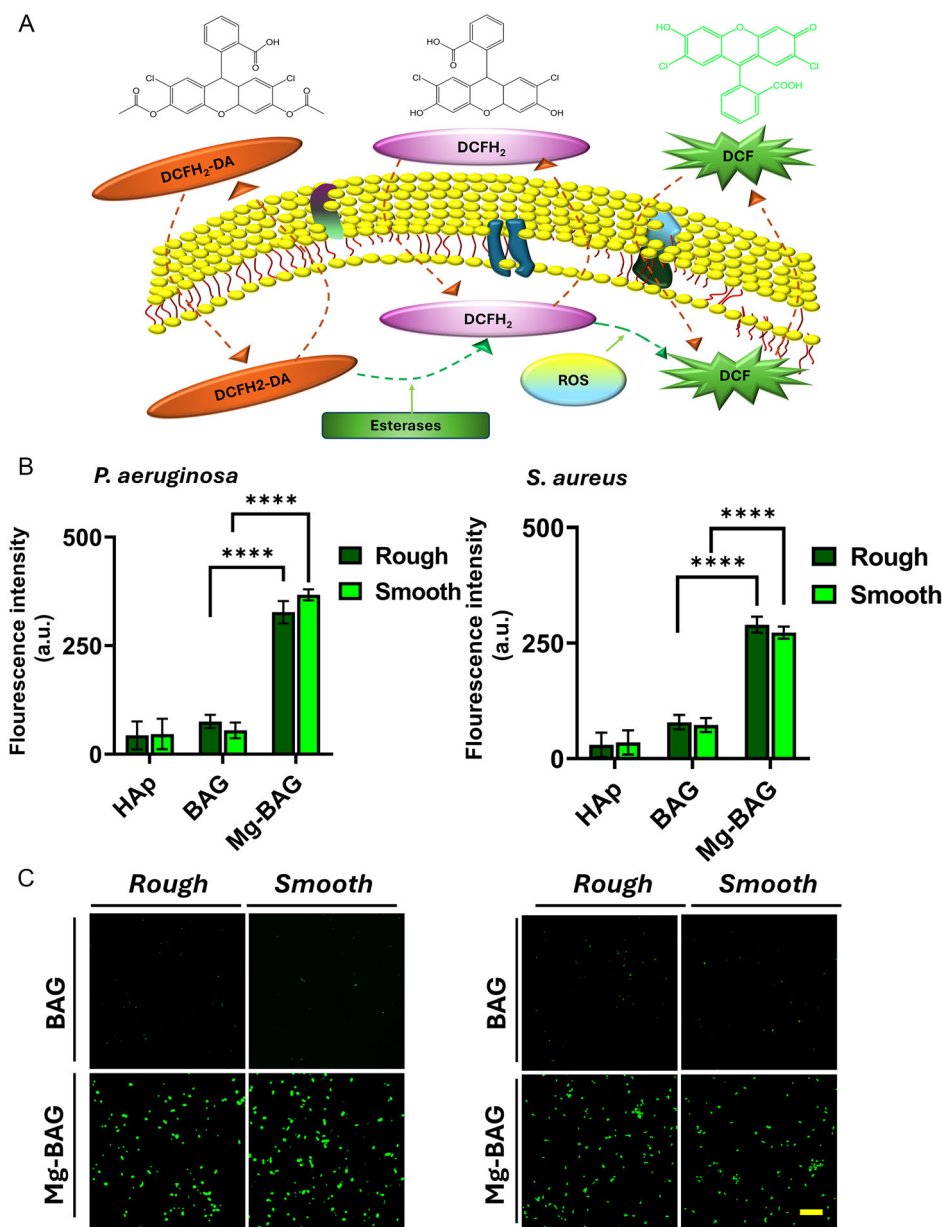


Figure 5. Intracellular ROS formation in *P. aeruginosa* and *S. aureus*. A) A schematic illustrating how the ROS detection assay works. The probe DCFH₂ DA enters the cells where intracellular esterases convert it into DCFH₂ which stays inside the cell. When it interacts with ROS, DCFH₂ is transformed into the fluorescent DCF allowing for the detection of ROS. B) Fluorescence measurements from CLSM images show the ROS produced in *P. aeruginosa* and *S. aureus*. Mg-BAG surfaces induce higher levels of ROS compared to HAP and BAG surfaces. The increase in ROS is likely due to the release of Mg²⁺ ions from the Mg-BAG stimulating reactions in the cells and causing stress. This ROS formation indicates oxidative damage, in the bacterial cells. C) CLSM images of *P. aeruginosa* and *S. aureus* on the surface. Green fluorescence indicates the presence of ROS. The scale bar represents 30 μm. *N* = 3 ± SD, *****p* < 0.0001.

normalization of the maps, a noticeable decrease in intensity was observed in the C-H, amide II, and nucleic acid regions after exposure to Mg-BAG. Additionally, the score plots (Figure 7C and 8C) demonstrated distinct differences between the *P. aeruginosa* and *S. aureus* groups on BAG and Mg-BAG surfaces. We performed principal component analysis (PCA) to compare bacteria on undoped BAG and Mg-BAG surfaces (Figure 7D and 8D). The PCA score for the principal

components, namely PC1, PC2, and PC3, would represent the linear combination of variables that best distinguish between the two groups. PC1 explains that most of the difference between the groups accounted for 95% of the difference between BAG and Mg-BAG. Similarly, for *S. aureus*, PC-1 accounted for 97% between BAG and Mg-BAG. This plot enabled the identification of absorption peaks representing noteworthy biomolecular differences, and the corresponding biomolecular compounds are

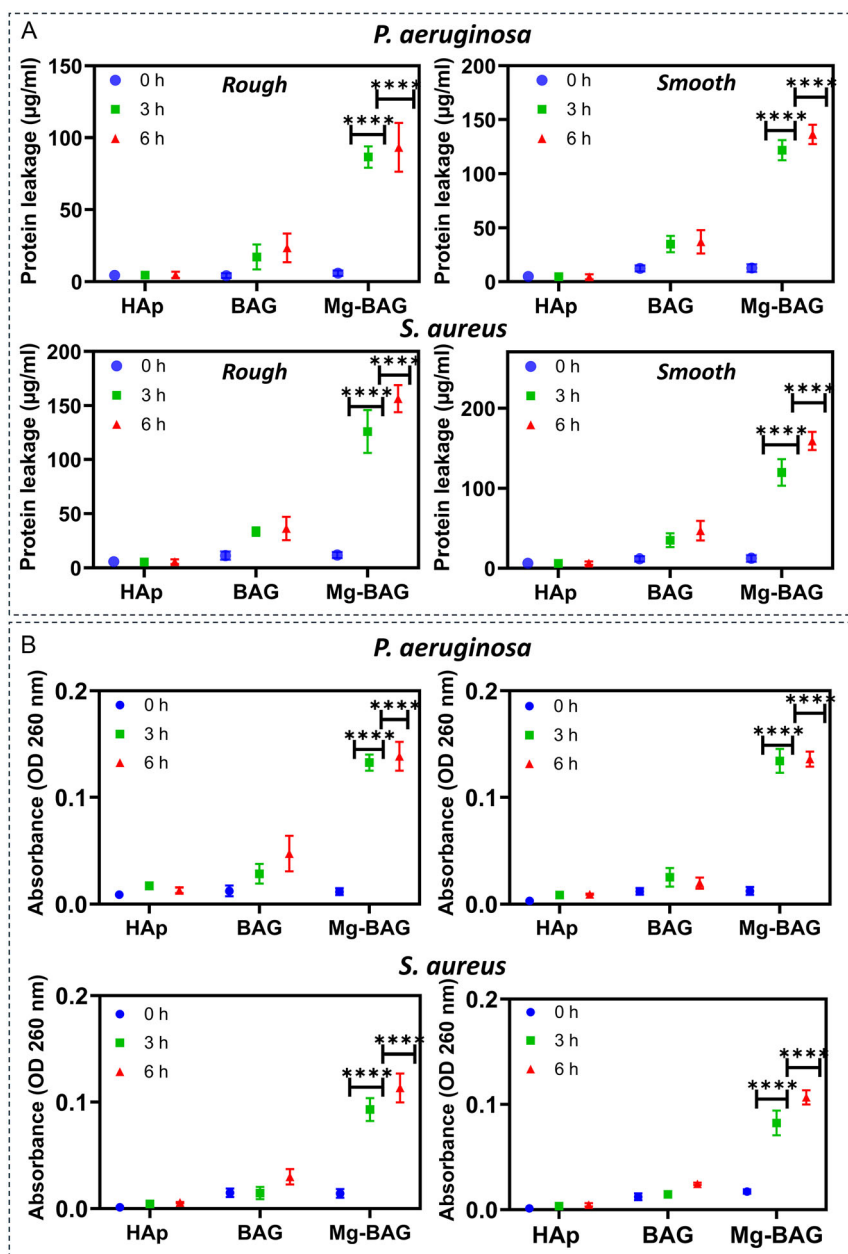


Figure 6. Quantitative assessment of the leakage of intracellular components from bacterial cells following incubation on Mg-BAG. A) Measurement of protein leakage from *P. aeruginosa* and *S. aureus* cells, reflecting the impact of these Mg-BAG on cellular membrane permeability and potential disruption of vital cellular processes. B) Evaluation of nucleic acid release from *P. aeruginosa* and *S. aureus* cells, indicating the extent of cellular membrane damage and the potential for compromised cellular integrity.

summarized in **Table 1**. Within the lipid region, changes to the methyl/methylene groups of the phospholipids within the cell membrane were observed, as evidenced by the peaks at 2925 and 2852 cm^{-1} . Most of the peaks in the PC-1 loadings were located in the amide bands, as indicated by the bands at 1954, 1637, 1514, 1452, and 1400 cm^{-1} . Changes in the 1236 and 1082 cm^{-1} bands demonstrated variations within the nucleic acid regions. These spectral changes suggest that biological damage has occurred at the molecular level. This damage can be

attributed to various factors, including oxidative stress and exposure to surface interactions with antibacterial agents. The observed biomolecular changes align with the effects of ion release, ROS formation, and membrane depolarization.

The lipid content, particularly phospholipids which are a dominant component of the bacterial membrane, is crucial for the structural integrity and function of the cell.^[42] These phospholipids can interact with metal cations with their reactive phosphoryl groups adjacent to carboxyl groups of unaltered lipids.^[43]

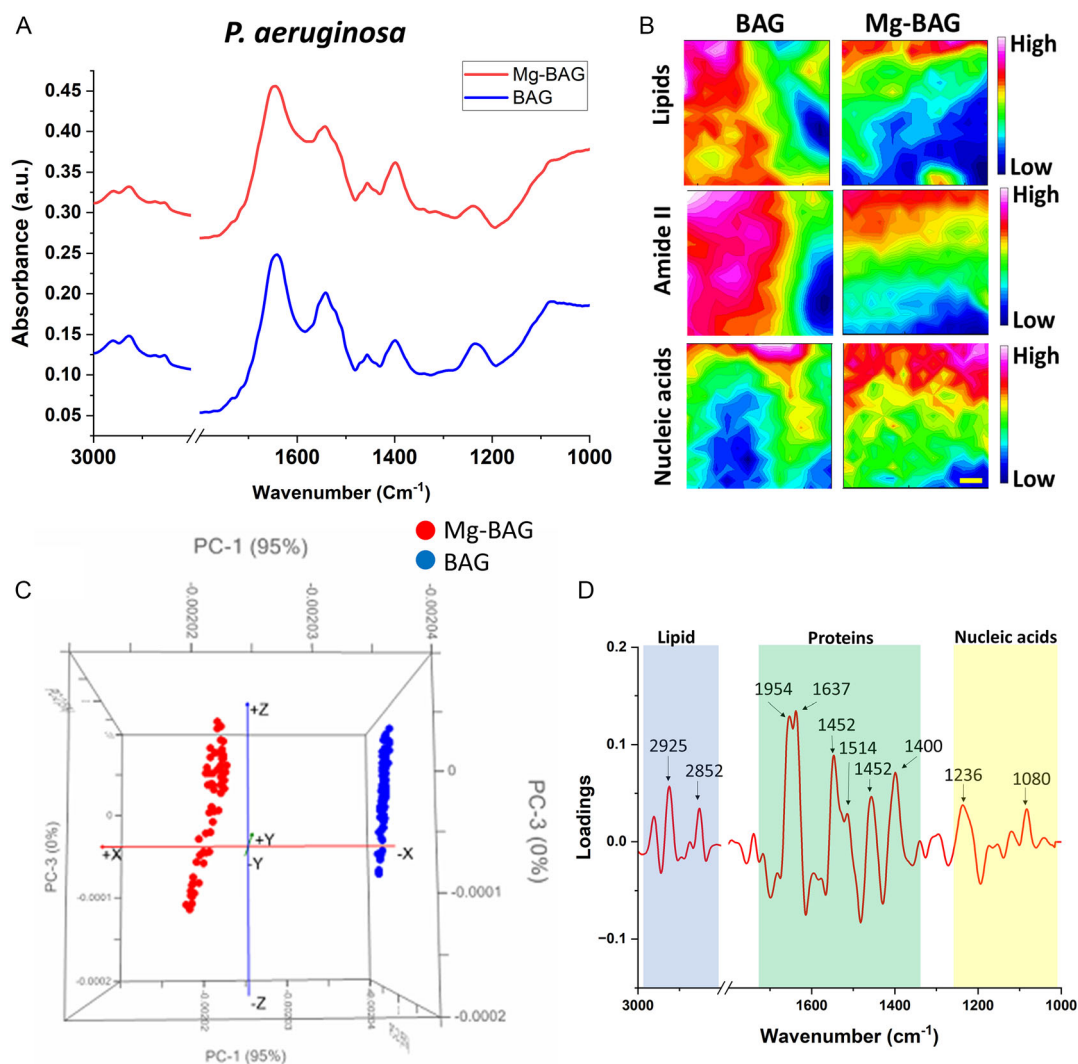


Figure 7. Synchrotron-sourced macro ATR-FTIR microscopy data identified biomolecular changes in *P. aeruginosa* after exposure to Mg-BAG. A) The average spectra from HCA. B) Synchrotron macro ATR-FTIR maps. The scale bar present 5 μm . C) The comparative PCA 3D score plots. D) PCA loading spectra for PC1.

In addition, metal ions trigger the oxidation of susceptible amino acids, thereby reducing protein stability, impairing function, and marking them for degradation.^[44] Changes in the spectra associated with protein peaks also make sense, considering the actions of oxidative stress upon cellular proteins. Proteins affected by oxidative stress can be unfolded, leaving them functionally inactive. This effect has repercussions for virtually all cellular metabolic processes, evidenced by the high rate of bacterial cell death. For example, the loss of membrane potential can be regarded as a direct repercussion of oxidative stress generated by the metal ions leached from Mg-BAG. Furthermore, various metal ions have been known to enhance ROS levels, which leads to nucleic acid damage.^[44,45] Our study represents the first account of how Mg-BAG can cause changes in the lipids of *P. aeruginosa* and *S. aureus*, disrupt protein synthesis or stability, and interfere with the genetic material of the bacteria.

Our Mg-BAG bioceramics exhibit significant antibacterial activity due to the release of magnesium ions (Mg^{2+}), which disrupt bacterial cell membranes, impairing ion homeostasis and leading to increased intracellular ROS production, ultimately causing bacterial cell death. Unlike other metal-doped biomaterials, Mg-BAG avoids cytotoxicity and inflammation, ensuring excellent biocompatibility. This biocompatibility is achieved through role of Mg^{2+} in stimulating osteoblast proliferation and differentiation, promoting bone formation by enhancing mineralization and supporting extracellular matrix development.

In addition to its antibacterial properties, Mg-BAG creates a favourable alkaline environment that supports bone regeneration while inhibiting the growth of pathogens. This dual functionality makes Mg-BAG particularly advantageous in bone tissue engineering, where it can act as both an infection-preventing agent and a regenerative scaffold.

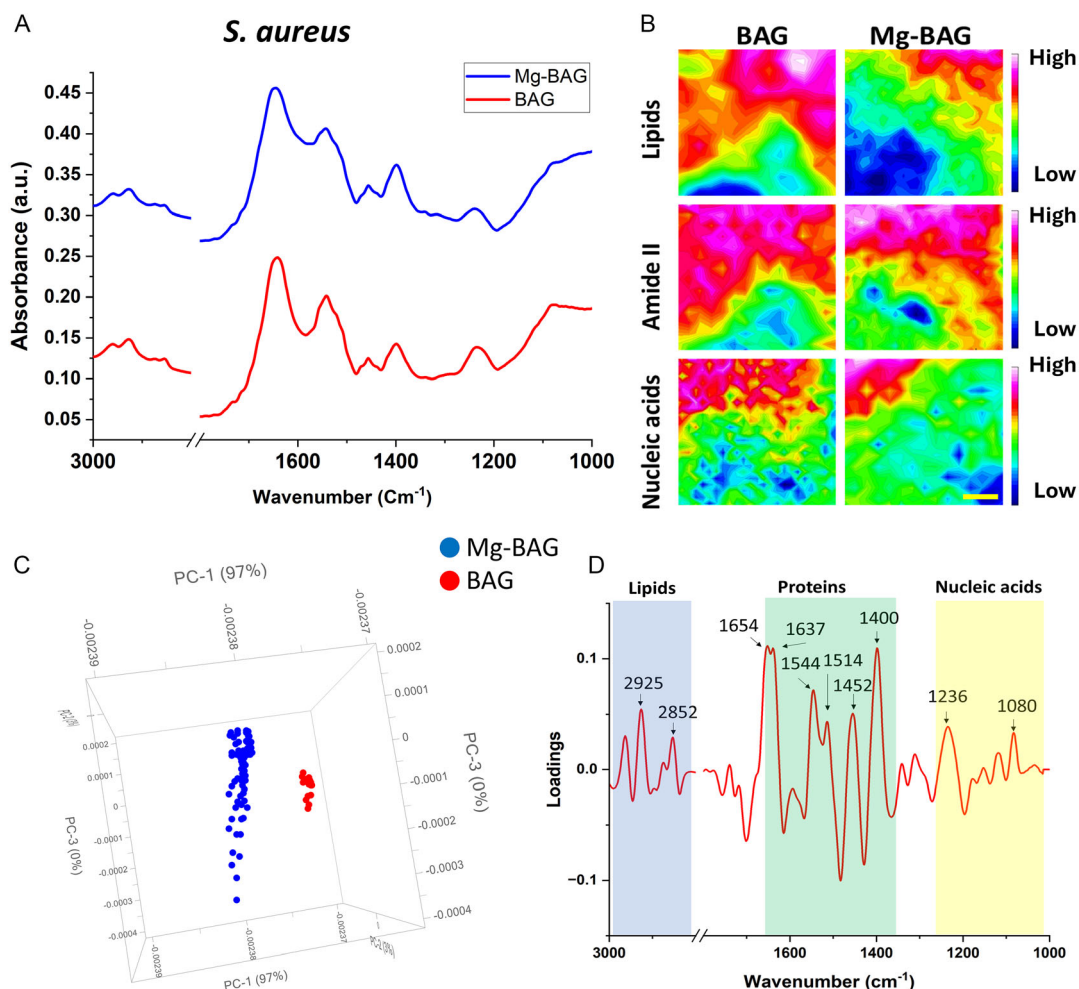


Figure 8. Synchrotron-sourced macro ATR-FTIR microscopy data identified biomolecular changes in *S. aureus* after exposure to Mg-BAG. A) The average spectra from HCA. B) Synchrotron macro ATR-FTIR. The scale bar presents 5 μm . C) The comparative PCA 3D score plots. D) PCA loading spectra for PC1.

Table 1. Summary of key wavenumbers for functional groups identified in the loading plots of *P. aeruginosa* and *S. aureus*.

Bacterial cell	Wavenumber (cm^{-1})	Assignment	References
<i>P. aeruginosa</i>	≈ 2925	$\nu_{\text{as}}(\text{C-H})$ from methylene ($-\text{CH}_2$) groups of lipids	[49]
and <i>S. aureus</i>	≈ 2852	$\nu_{\text{s}}(\text{C-H})$ from methylene ($-\text{CH}_2$) groups of lipids	[49,50]
	≈ 1654	Amide I: α -helix	[49]
	≈ 1637	Amide I: antiparallel β -sheet	[51]
–	$\approx 1452\text{--}1514$	C–H stretching of CH_2 and CH_3 groups in cellular proteins, nucleic acids and lipids	[49]
	≈ 1452	$\delta_{\text{as}}(\text{CH}_3)$ of proteins (possibly in DNA and RNA)	[49]
	≈ 1400	$\nu_{\text{s}}(\text{COO}^-)$ associated with $\delta_{\text{s}}(\text{CH}_3)$ of proteins	[49]
	≈ 1236	$\nu_{\text{as}}(\text{PO}_4^{2-})$ of DNA	[52]
–	≈ 1080	$\nu_{\text{s}}(\text{PO}_4^{2-})$ of the phosphodiester backbone of nucleic acids (DNA and RNA) and phospholipids	[49]

These findings suggest that Mg-BAG is a promising multi-functional implant technology that can enhance the success rate of bone regeneration therapies by simultaneously promoting tissue integration and preventing infections. Balancing

antibacterial activity with bone regenerative properties opens new avenues for designing Mg-BAG-coated implants or scaffolds that could significantly reduce infection risks and improve patient outcomes.

3. Conclusion

In this study, we have successfully engineered the baghdadite by doping it with Mg to impart antibacterial properties to the material. Our finding demonstrates the synergistic and broad-spectrum antibacterial activity of Mg-BAG against both clinically relevant pathogens Gram-negative *P. aeruginosa* and Gram-positive *S. aureus*. We have elucidated the multifaceted antibacterial mechanisms by analyzing cell morphology, ROS formation, membrane potential, leakage of cell contents, and biomolecular changes. This study represents a breakthrough in our understanding of Mg baghdadite, highlighting their potential as next-generation multifunctional bioceramics for bone regeneration applications.

4. Experimental Section

Fabrication and Characterizations of Mg-BAG: HAp, BAG, and Mg-BAG discs were prepared following steps presented in a previous study using a solid-state synthesis route.^[12,13] The powders were mixed for 1 h at 100 rpm for BAG and 5 h at 200 rpm for Mg-BAG using a planetary ball mill (PM400 Retsch, Germany). After homogenization, the obtained mixture was calcined in an electric furnace (RHF, Carbolite UK) at 1300 °C of Mg-BAG for 1350 °C of BAG. For the preparation of the discs, the calcined powders were ground in the planetary ball mill for 3 h at 150 rpm and then uniaxially pressed at 300 MPa to obtain disc-shaped green bodies. These were then sintered in an electric furnace (RHF, Carbolite UK) at 1300 °C of Mg-BAG and 1350 °C of BAG to obtain disc samples. Surface topography evaluation was conducted using optical 3D profilometry. The average roughness (Ra) was used in this study. The elemental distribution diagrams were obtained through energy-dispersive XPS (A Thermo Scientific K-alpha and analyzed with CasaXPS software).

Cultures and Conditions: HAp, BAG, and Mg-BAG were tested for antibacterial activity against two bacterial strains: *P. aeruginosa* (ATCC 15 692) and *S. aureus* (ATCC 25 923). Bacterial strains were recovered from glycerol stocks stored at –80 °C and streaked for purity on tryptone soy agar (TSA). One isolated colony of each species was transferred aseptically from TSA to 5 mL of tryptone soy broth (TSB) and cultured at 37 °C until the late log phase (≈6–8 h). Baghdadite and doped baghdadite samples were aseptically placed in sterile 24-well plates and immersed in 0.5 mL of the 10⁵ CFU mL⁻¹ bacterial suspensions and then incubated for 3 or 6 h.

Live/Dead BacLight Viability Assay: Confocal laser scanning microscopic (CLSM) was used to visualize and quantify the proportions of live and dead cells using the LIVE/DEAD BacLight Bacterial Viability Kit (Molecular Probes, Invitrogen, USA), which contains SYTO9 and propidium iodide fluorescent dyes. SYTO9 enters all cells, binding to nucleic acids and fluorescing green. Propidium iodide (PI) only enters cells with disrupted membranes and has a stronger affinity for nucleic acids than SYTO9. PI fluoresces red and indicates dead or viable cells.^[46] SYTO9 and PI were prepared in equal proportions at 1.5 μL mL⁻¹ in phosphate-buffered saline (PBS), and 1 mL of the solution was used to immerse each sample for 15 min in the dark at room temperature. After staining, samples were imaged with a Zeiss_LSM880 (Zeiss, Oberkochen, Germany) CLSM. Using a dual-emission filter, the CLSM was set up to image both live cells in green (Syto9, Ex/Em 480/500 nm) and dead cells in red (PI, Ex/Em 490/635 nm).

Colony Enumeration: The colony-forming unit (CFU) determination and log reduction data (Figure S2, Supporting Information) were performed. Following incubation, sample discs were vortexed in PBS for 15 s, then sonicated for 5 min before being vortexed for another 15 s, and serially (1:10) diluted. In triplicate, serially diluted samples (10 μL) were dropped onto TSA plates and incubated for 18 h at 37 °C. Viability assays were performed by standard plate counts, and the quantity of CFU per sample was calculated using the number of colonies counted, the aliquot size, and the

dilution factor. A log reduction value was calculated for the two sample types (BAG, Mg-BAG) compared to a HAp control.

Zone of Inhibition: Bacterial lawn plates were prepared by transferring 100 μL aliquots of bacterial cell suspension (at 1 × 10⁵ CFU mL⁻¹) onto a TSA plate and then evenly spreading it across the surface. Untreated and doped baghdadite discs were aseptically placed in defined quadrants of the plate and left to incubate overnight at 37 °C. The following day, the inhibition zones were measured by recording the radius from the center of the disc to the perimeter of the clear zone of inhibition.

SEM Characterization of Bacterial Morphology on the Surface: SEM was used to observe the morphological changes according to previous studies.^[47] Disc samples were cultured with bacteria (≈1 × 10⁵ CFU mL⁻¹) and incubated in TSB medium at 37 °C for 3 and 6 h. After incubation, all discs were washed twice with PBS (pH 7.4) to remove unattached cells. The bacterial cells were fixed in 4% glutaraldehyde for 1 h at room temperature. The samples were dehydrated in sequential graded ethanol (30%, 50%, 70%, 90%, 100%). Finally, all samples were coated with 2 nm platinum. Samples were then observed in a FEI Inspect F50 (FEI Company, Oregon, USA) at 5 kV with a working distance of 5 mm.

Ions Release Analysis: To assess the release of Mg ions from the Mg-BAG samples, we immersed the samples in 0.5 mL of TSB media at 37 °C for 3 and 6 h. After incubation, the supernatants were collected and centrifuged to remove debris or particles. The supernatants were then treated with HNO₃ to dissolve any remaining solids and diluted to a concentration of less than 5% to avoid matrix effects during ICP-MS analysis. The concentration of Mg ions in the supernatants was measured using ICP-MS with a Varian 720-ES system from the United States. Standard solutions of known concentrations were prepared to calibrate the instrument before the analysis. The concentration of Mg ions in the samples was determined using the standard curve generated from the standards.

The ROS-Level Determination: To investigate the ROS levels in target bacteria, we used an intercellular ROS formation assessed using a DCFDA/H2DCFDA- Cellular ROS Assay Kit (ab113851, Abcam, USA). Following incubation with HAp, BAG, and Mg-BAG samples, bacteria were incubated with DCFH-DA (50 μM) in the dark for 30 min according to the manufacturer's instructions. The samples were then immediately imaged with a Zeiss_LSM880 CLSM using Ex/Em of 485/535 nm. Images were taken at three random locations per sample. The fluorescence intensity of each image was then determined using ImageJ v1.53a (NIH, Maryland, USA). The ROS level was calculated based on the fluorescence intensity of the DCF, which was converted to a highly fluorescent compound by ROS. Higher fluorescence intensity indicates higher ROS levels in the bacterial cells.

Determination of Cell Membrane Potentials: Following incubation, the membrane potential of bacterial cells was measured using the BacLight Bacterial Membrane Potential Kit (Invitrogen, ThermoFisher, Massachusetts, USA). The staining procedure was carried out according to the instructions of the manufacturer. The samples were then immediately imaged using a Zeiss_LSM880 CLSM, Ex/Em 482/497 nm. Three micrographs were taken randomly, and the images were imported into ImageJ v1.53a. Fluorescence intensity was measured in the green and red channels, and a red-to-green ratio was calculated using the acquired intensities.

Leakage of Intracellular Nucleic Acids and Proteins: Following incubation on the baghdadite and doped baghdadite samples for 3 and 6 h, we measured the optical density of the supernatant at 260 nm to quantify the nucleic acid content. The BCA (bicinchoninic acid) assay is commonly used for measuring protein concentration. To use this assay, a standard curve was first generated using known concentrations of a protein standard, such as bovine serum albumin. Protein samples and the BCA working reagent were added to a 96-well microplate. After incubating the plate for a specific amount of time at 37 °C, the absorbance of each well was measured at a specific wavelength using a microplate reader. The protein concentration in the sample was determined by comparing the absorbance of the sample to the standard curve. Using a microplate reader to measure the absorbance of the samples allows for quick and accurate determination of the protein concentration in each well of the plate.

Synchrotron Macro-ATR-FTIR: To study the biochemical changes in bacterial cells exposed to BAG and Mg-BAG samples, we used synchrotron

ATR-FTIR microspectroscopy at Australian Synchrotron.^[48] Bacterial cells were grown and treated according to the previous experimental design for 6 h with the smooth group of BAG, Mg-BAG samples, after which they were collected and deposited onto the ATR crystal of the synchrotron microscope. ATR-FTIR spectra were then collected across the 3400–1000 cm⁻¹ spectral range, allowing for the identification and quantification of various molecular vibrations and functional groups. The resulting spectra were then analyzed using various chemometric methods, such as hierarchical clustering analysis (HCA), second derivative spectroscopy, and PCA, to identify changes in the biochemical composition of the bacteria. HCA was used for quality control and to identify outlier spectra, while second-derivative spectroscopy enhanced the resolution of overlapping peaks. PCA was used to explore the treatment groups' clustering patterns and chemical composition differences.

Statistical Analyses: Statistical Significance Was Evaluated Using One-Way Analysis of Variance with Tukey's Multiple Comparisons Test. *p*-Value < 0.05 Was Considered Statistically Significant. All Experiments Were Performed in Triplicate and Data Were Presented as Mean and SD.

Supporting Information

Supporting Information is available from the Wiley Online Library or from the author.

Acknowledgements

The authors acknowledge the Australia National Health and Medical Research Council (NHMRC), the Australian Research Council, the synchrotron-FTIR measurement was undertaken on the Infrared Microspectroscopy (IRM) beamline at the Australian Synchrotron, part of ANSTO. The authors would like to express their gratitude to the Flinders Microscopy and Microanalysis, Flinders Analytical, and Adelaide Microscopy for their assistance with the microscopy work conducted in this study. This work was funded by Khalifa University (grant no. RC2-2018-022 to V.K.T.). K.V. thanks NHMRC for Fellowship GNT1194466. The authors extend their sincere gratitude to Professor David Stopar and Assistant Professor Iztok Dogsa from the University of Ljubljana and Dr Kim Chung Nguyen and Ta Xuan Minh Chau from The University of Sydney for their invaluable comments. Their expertise and thoughtful insights greatly contributed to the advancement of our work.

Conflict of Interest

The authors declare no conflict of interest.

Author Contributions

Ngoc Huu Nguyen: Conceptualization (lead); Data curation (lead); Formal analysis (lead); Methodology (equal); Validation (lead); Visualization (lead); Writing—original draft (lead); Writing—review and editing (lead). **Iman Roohani:** Conceptualization (supporting); Data curation (supporting); Methodology (equal); Supervision (supporting); Validation (supporting); Visualization (supporting); Writing—original draft (supporting); Writing—review and editing (supporting). **Andrew Hales:** Formal analysis (supporting); Methodology (supporting); Visualization (supporting); Writing—original draft (supporting); Writing—review and editing (supporting). **Zufu Lu:** Conceptualization (supporting); Data curation (supporting); Methodology (equal); Supervision (supporting); Validation (supporting); Visualization (supporting); Writing—original draft (supporting); Writing—review and editing (supporting). **Jitraporn Vongsvivut:** Formal analysis (supporting); Methodology (supporting); Visualization (supporting); Writing—original draft (supporting); Writing—review and editing (supporting). **Krasimir Vasilev:**

Conceptualization (supporting); Funding acquisition (supporting); Methodology (supporting); Supervision (supporting); Writing—original draft (supporting); Writing—review and editing (supporting). **Vi Khanh Truong:** Conceptualization (lead); Formal analysis (lead); Funding acquisition (lead); Investigation (lead); Methodology (lead); Resources (lead); Supervision (lead); Writing—original draft (equal); Writing—review and editing (equal). **Hala Zreiqat:** Funding acquisition (lead); Investigation (lead); Methodology (lead) Project administration (lead); Resources (lead); Supervision (lead); Visualization (lead); Writing—original draft (supporting); Writing—review and editing (supporting).

Data Availability Statement

The data that support the findings of this study are available from the corresponding author upon reasonable request.

Keywords

baghdadites, Calcium-silicate-based ceramics, implant infections, magnesium, orthopedics, *Pseudomonas aeruginosa*, *Staphylococcus aureus*

Received: August 2, 2024

Revised: October 1, 2024

Published online:

- [1] C. T. Johnson, A. J. Garcia, *Ann. Biomed. Eng.* **2015**, *43*, 515.
- [2] A. Trampuz, A. F. Widmer, *Curr. Opin. Infect. Dis.* **2006**, *19*, 349.
- [3] a) C. R. Arciola, D. Campoccia, L. Montanaro, *Nat. Rev. Microbiol.* **2018**, *16*, 397; b) A. T. Nguyen, A. G. Oglesby-Sherrouse, *Appl. Microbiol. Biotechnol.* **2016**, *100*, 6141; c) E. A. Masters, B. F. Ricciardi, K. L. D. M. Bentley, T. F. Moriarty, E. M. Schwarz, G. Muthukrishnan, *Nat. Rev. Microbiol.* **2022**, *20*, 385.
- [4] M. Vallet-Regí, D. Lozano, B. González, I. Izquierdo-Barba, *Adv. Healthcare Mater.* **2020**, *9*, 2000310.
- [5] K. Hansson, A. Brenthel, *Med. Humanit.* **2022**, *48*, 381.
- [6] B. Aslam, M. Ahmad, M. U. Tariq, S. Muzammil, A. B. Siddique, M. Khurshid, A. Shahid, M. H. Rasool, T. H. Chaudhry, A. Amir, *Degradation of Antibiotics and Antibiotic-Resistant Bacteria from Various Sources*, Elsevier, Amsterdam, New York **2023**.
- [7] a) S. Roohani-Esfahani, C. Dunstan, B. Davies, S. Pearce, R. Williams, H. Zreiqat, *Acta Biomater.* **2012**, *8*, 4162; b) J. J. Li, A. Akey, C. R. Dunstan, M. Viereicher, O. Friedrich, D. C. Bell, H. Zreiqat, *Adv. Healthcare Mater.* **2018**, *7*, 1800218; c) G. A. Nasser Atia, H. R. Barai, H. K. Shalaby, N. G. Ali, S. M. Morsy, M. M. Ghobashy, H. A. Nasser Attia, S. W. Joo, *ACS Omega* **2022**, *7*, 44532; d) S. Sadeghzade, J. Liu, H. Wang, X. Li, J. Cao, H. Cao, H. Yuan, *Mater. Today Bio* **2022**, *17*, 100473; e) Z. Lu, W. Zhang, Y. J. No, Y. Lu, S. M. Mirkhalaf Valashani, P. Rollet, L. Jiang, Y. Ramaswamy, C. R. Dunstan, X. Jiang, *ACS Biomater. Sci. Eng.* **2020**, *6*, 6874.
- [8] a) J. L. Hobman, L. C. Crossman, *J. Med. Microbiol.* **2015**, *64*, 471; b) A. Evans, K. A. Kavanagh, *J. Med. Microbiol.* **2021**, *70*.
- [9] W. K. Jung, H. C. Koo, K. W. Kim, S. Shin, S. H. Kim, Y. H. Park, *Appl. Environ. Microbiol.* **2008**, *74*, 2171.
- [10] J. Wu, L. Wang, J. He, C. Zhu, *Contraception* **2012**, *85*, 509.
- [11] E. Woods, C. Cochrane, S. Percival, *Vet. Microbiol.* **2009**, *138*, 325.
- [12] M. Mirkhalaf, J. Goldsmith, J. Ren, A. Dao, P. Newman, A. Schindeler, M. A. Woodruff, C. R. Dunstan, H. Zreiqat, *Appl. Mater. Today* **2021**, *25*, 101230.
- [13] a) Y. J. No, T. Nguyen, Z. Lu, M. Mirkhalaf, F. Fei, M. Foley, H. Zreiqat, *Bone* **2021**, *153*, 116147; b) J. J. Li, S.-I. Roohani-

- Esfahani, C. R. Dunstan, T. Quach, R. Steck, S. Saifzadeh, P. Pivonka, H. Zreiqat, *Biomed. Mater.* **2016**, *11*, 015016.
- [14] a) K. Sinulingga, M. Sirait, N. Siregar, M. E. Doloksaribu, *ACS Omega* **2021**, *6*, 34185; b) D. Predoi, S. L. Iconaru, M. V. Predoi, G. E. Stan, N. Buton, *Nanomaterials* **2019**, *9*, 1295; c) Q. Bi, X. Song, Y. Chen, Y. Zheng, P. Yin, T. Lei, *Colloids Surf., B* **2020**, *189*, 110813; d) G. Ciobanu, M. Harja, *Nanomaterials* **2019**, *9*, 1696; e) Y. Li, G. Liu, Z. Zhai, L. Liu, H. Li, K. Yang, L. Tan, P. Wan, X. Liu, Z. Ouyang, *Antimicrob. Agents Chemother.* **2014**, *58*, 7586; f) J. Rodríguez-Sánchez, M. Á. Pacha-Olivenza, M. L. González-Martín, *Mater. Chem. Phys.* **2019**, *221*, 342.
- [15] M. Ribeiro, F. J. Monteiro, M. P. Ferraz, *Biomatter* **2012**, *2*, 176.
- [16] a) R. A. Gittens, T. McLachlan, R. Olivares-Navarrete, Y. Cai, S. Berner, R. Tannenbaum, Z. Schwartz, K. H. Sandhage, B. D. Boyan, *Biomaterials* **2011**, *32*, 3395; b) O. Andrukhov, R. Huber, B. Shi, S. Berner, X. Rausch-Fan, A. Moritz, N. D. Spencer, A. Schedle, *Dent. Mater.* **2016**, *32*, 1374.
- [17] a) D. Perera-Costa, J. M. Bruque, M. L. González-Martín, A. C. Gómez-García, V. Vadillo-Rodríguez, *Langmuir* **2014**, *30*, 4633; b) L. C. Hsu, J. Fang, D. A. Borca-Tasciuc, R. W. Worobo, C. I. Moraru, *Appl. Environ. Microbiol.* **2013**, *79*, 2703; c) C. Zhao, X. Wang, L. Gao, L. Jing, Q. Zhou, J. Chang, *Acta Biomater.* **2018**, *73*, 509; d) R. Sorrentino, A. Cochis, B. Azzimonti, C. Caravaca, J. Chevalier, M. Kuntz, A. A. Porporati, R. M. Streicher, L. Rimondini, *J. Eur. Ceram. Soc.* **2018**, *38*, 963.
- [18] a) I. Yoda, H. Koseki, M. Tomita, T. Shida, H. Horiuchi, H. Sakoda, M. Osaki, *BMC Microbiol.* **2014**, *14*, 234; b) S. Senevirathne, J. Hasan, A. Mathew, M. Woodruff, P. Yarlagadda, *RSC Adv.* **2021**, *11*, 1883.
- [19] G. Mi, D. Shi, M. Wang, T. J. Webster, *Adv. Healthcare Mater.* **2018**, *7*, 1800103.
- [20] a) D. P. Linklater, V. A. Baulin, S. Juodkazis, R. J. Crawford, P. Stoodley, E. P. Ivanova, *Nat. Rev. Microbiol.* **2021**, *19*, 8; b) G. Mendonça, D. B. Mendonça, F. J. Aragao, L. F. Cooper, *Biomaterials* **2008**, *29*, 3822; c) S. V. Oopath, A. Baji, M. Abtahi, T. Q. Luu, K. Vasilev, V. K. Truong, *Adv. Mater. Interfaces* **2023**, *10*, 2201425.
- [21] M. Berney, F. Hammes, F. Bosshard, H.-U. Weilenmann, T. Egli, *Appl. Environ. Microbiol.* **2007**, *73*, 3283.
- [22] a) N. Iqbal, M. R. A. Kadir, N. A. N. Malek, N. H. Mahmood, M. R. Murali, T. Kamarul, *Mater. Lett.* **2012**, *89*, 118; b) M. Balouiri, M. Sadiki, S. K. Ibsouda, *J. Pharm. Anal.* **2016**, *6*, 71.
- [23] E. R. Chellaiah, *Appl. Water Sci.* **2018**, *8*, 154.
- [24] M. J. Sullivan, K. G. Goh, G. C. Ulett, *PLoS Pathog.* **2022**, *18*, e1010607.
- [25] a) O. McNeilly, R. Mann, M. Hamidian, C. Gunawan, *Front. Microbiol.* **2021**, *12*, 652863; b) S. Silver, A. Gupta, K. Matsui, J.-F. Lo, *Met.-Based Drugs* **1999**, *6*, 315; c) E. Terzioğlu, M. Arslan, B. G. Balaban, Z. P. Çakar, *World J. Microbiol. Biotechnol.* **2022**, *38*, 158.
- [26] C. L. Dupont, G. Grass, C. Rensing, *Metalomics* **2011**, *3*, 1109.
- [27] Y. Liu, B. Rath, M. Tingart, J. Eschweiler, *J. Biomed. Mater. Res. Part A* **2020**, *108*, 470.
- [28] S. Zheng, M. Bawazir, A. Dhall, H.-E. Kim, L. He, J. Heo, G. Hwang, *Front. Bioeng. Biotechnol.* **2021**, *9*, 643722.
- [29] Y. Huang, G. Zha, Q. Luo, J. Zhang, F. Zhang, X. Li, S. Zhao, W. Zhu, X. Li, *Sci. Rep.* **2014**, *4*, 6172.
- [30] Y. Wang, W. Teng, Z. Zhang, X. Zhou, Y. Ye, P. Lin, A. Liu, Y. Wu, B. Li, C. Zhang, *Bioact. Mater.* **2021**, *6*, 1853.
- [31] a) R. J. Doyle, T. H. Matthews, U. Streips, *J. Bacteriol.* **1980**, *143*, 471; b) R. Biswas, U. Halder, A. Kabiraj, A. Mondal, R. Bandopadhyay, *Arch. Microbiol.* **2021**, *203*, 2761.
- [32] J. P. Morth, B. P. Pedersen, M. J. Buch-Pedersen, J. P. Andersen, B. Vilsen, M. G. Palmgren, P. Nissen, *Nat. Rev. Mol. Cell Biol.* **2011**, *12*, 60.
- [33] M. S. Khater, G. R. Kulkarni, S. S. Khater, H. Gholap, R. Patil, *Mater. Res. Express* **2020**, *7*, 035005.
- [34] K. R. Messner, J. A. Imlay, *J. Biol. Chem.* **1999**, *274*, 10119.
- [35] a) S. Korshunov, J. A. Imlay, *Mol. Microbiol.* **2010**, *75*, 1389; b) N. Mammari, E. Lamouroux, A. Boudier, R. E. Duval, *Microorganisms* **2022**, *10*, 437; c) J. A. Imlay, *Nat. Rev. Microbiol.* **2013**, *11*, 443.
- [36] A. A. Vitale, E. A. Bernatene, M. G. Vitale, A. B. Pomilio, *J. Phys. Chem. A* **2016**, *120*, 5435.
- [37] V. Luque-Agudo, M. C. Fernández-Calderón, M. A. Pacha-Olivenza, C. Perez-Giraldo, A. M. Gallardo-Moreno, M. L. González-Martín, *Colloids Surf., B* **2020**, *191*, 110996.
- [38] A. Truskewycz, V. K. Truong, A. S. Ball, S. Houshyar, N. Nassar, H. Yin, B. J. Murdoch, I. Cole, *ACS Appl. Mater. Interfaces* **2021**, *13*, 27904.
- [39] C. J. Ioannou, G. W. Hanlon, S. P. Denyer, *Antimicrob. Agents Chemother.* **2007**, *51*, 296.
- [40] a) J. Anastassopoulou, T. Theophanides, in *Bioinorganic Chemistry: An Inorganic Perspective of Life* (Ed: D. P. Kessissoglou) Springer Netherlands, Dordrecht **1995**; b) L. Li, L. Cao, X. Xiang, X. Wu, L. Ma, F. Chen, S. Cao, C. Cheng, D. Deng, L. Qiu, *Adv. Funct. Mater.* **2022**, *32*, 2107530.
- [41] a) Z. Shaw, S. Cheeseman, L. Z. Huang, R. Penman, T. Ahmed, S. J. Bryant, G. Bryant, A. J. Christofferson, R. Orrell-Trigg, C. Dekiwadia, *J. Mater. Chem. B* **2022**, *10*, 7527; b) X.-J. Hu, Z.-X. Liu, Y.-D. Wang, X.-L. Li, J. Hu, J.-H. Lü, *Nucl. Sci. Tech.* **2016**, *27*, 56; c) S. Cheeseman, V. K. Truong, J. Vongsvivut, M. J. Tobin, R. Crawford, E. P. Ivanova, *Synchrotron Radiation-Useful and Interesting Applications*, Intechopen **2019**, <http://dx.doi.org/10.5772/intechopen.79284>.
- [42] a) S. Kumar, A. Mollo, D. Kahne, N. Ruiz, *Chem. Rev.* **2022**, *122*, 8884; b) R. Kulkarni, E. A. Wiemer, W. Chang, *Front. Immunol.* **2022**, *12*, 815020.
- [43] J. M. Pettersen, Y. Yang, A. S. Robinson, *Trends Biotechnol.* **2023**, *41*, 1041.
- [44] M. Godoy-Gallardo, U. Eckhard, L. M. Delgado, Y. J. de Roo Puente, M. Hoyos-Nogués, F. J. Gil, R. A. Perez, *Bioact. Mater.* **2021**, *6*, 4470.
- [45] J. Díaz-Visurraga, C. Gutiérrez, C. Von Plessing, A. García, *Sci. Against Microbiol. Pathog.* **2011**, *1*, 210.
- [46] E. P. Ivanova, J. Hasan, H. K. Webb, G. Gervinkas, S. Juodkazis, V. K. Truong, A. H. Wu, R. N. Lamb, V. A. Baulin, G. S. Watson, *Nat. Commun.* **2013**, *4*, 2838.
- [47] D. Q. Pham, S. Gangadoo, C. C. Berndt, J. Chapman, J. Zhai, K. Vasilev, V. K. Truong, A. S. M. Ang, *ACS Appl. Mater. Interfaces* **2022**, *14*, 18974.
- [48] J. Vongsvivut, D. Pérez-Guaita, B. R. Wood, P. Heraud, K. Khambatta, D. Hartnell, M. J. Hackett, M. J. Tobin, *Analyst* **2019**, *144*, 3226.
- [49] a) J. Vongsvivut, P. Heraud, A. Gupta, M. Puri, D. McNaughton, C. J. Barrow, *Analyst* **2013**, *138*, 6016; b) J. Ojeda, M. Romero-Gonzalez, H. Pouran, S. Banwart, *Mineral. Mag.* **2008**, *72*, 101.
- [50] U. Bocker, R. Ofstad, Z. Wu, H. Bertram, G. Sockalingum, M. Manfait, *Appl. Spectrosc.* **2007**, *61*, 1032.
- [51] a) S. J. Parikh, J. Chorover, *Langmuir* **2006**, *22*, 8492; b) Z. Movasaghi, S. Rehman, D. I. ur Rehman, *Appl. Spectrosc. Rev.* **2008**, *43*, 134.
- [52] a) B. R. Wood, *Chem. Soc. Rev.* **2016**, *45*, 1980; b) R. C. Tomas, A. J. Sayat, A. N. Atienza, J. L. Danganan, M. R. Ramos, A. Fellizar, K. I. Notarte, L. M. Angeles, R. Bangaol, A. Santillan, *PLoS One* **2022**, *17*, e0262489.